JACS
JOURNAL OF THE AMERICAN CHEMICAL SOCIETY

Communication

pubs.acs.org/JACS

Heazlewoodite, Ni_3S_2: A Potent Catalyst for Oxygen Reduction to Water under Benign Conditions

Joseph M. Falkowski, Nolan M. Concannon, Bing Yan, and Yogesh Surendranath*

Department of Chemistry, Massachusetts Institute of Technology, 77 Massachusetts Avenue, Cambridge, Massachusetts 02139-4307, United States

Supporting Information

ABSTRACT: Electrodeposited thin films and nanoparticles of Ni_3S_2 are highly active, poison- and corrosion-resistant catalysts for oxygen reduction to water at neutral pH. In pH 7 phosphate buffer, Ni_3S_2 displays catalytic onset at 0.8 V versus the reversible hydrogen electrode, a Tafel slope of 109 mV decade^{-1}, and high faradaic efficiency for four-electron reduction of O_2 to water. Under these conditions, the activity and stability of Ni_3S_2 exceeds that of polycrystalline platinum and manganese, nickel, and cobalt oxides, illustrating the catalytic potential of pairing labile first-row transition metal active sites with a more covalent sulfide host lattice.

The interconversion of water and O_2 is an essential chemistry underlying a future renewable energy economy.[1] Nature executes this kinetically demanding multiproton, multielectron interconversion with remarkable selectivity and efficiency. Oxygen evolution is carried out at the Mn_4Ca cofactor of the oxygen evolving complex of photosystem II,[2] whereas oxygen reduction is carried out at the heme/Cu active site of cytochrome C oxidase[3] and Cu_3 cluster active sites of multicopper oxidases.[4] Although these catalysts operate efficiently and selectively under benign conditions of neutral pH and ambient temperature and pressure, precious and base metal-containing heterogeneous catalysts typically require highly alkaline or acidic electrolytes (Figure 1).

The paucity of heterogeneous electrocatalysts capable of efficient oxygen reduction at neutral pH[5] arises from two seemingly divergent kinetic/materials requirements: (1) The catalyst must remain active in the presence of buffering electrolytes that are required to maintain neutral pH stability and deliver protons to drive the proton-coupled electron transfer (PCET) activation of O_2.[6] (2) The catalyst must resist protolytic corrosion under reducing conditions. Precious-metal catalysts such as Pt and Au meet the latter requirement but also strongly adsorb buffering electrolyte ions such as phosphate, degrading their catalytic efficiency.[7] In contrast, low valent mid-to-late first-row transition metal ions are substitutionally labile,[8] allowing them to meet the first requirement, but this very property makes their corresponding oxides unstable with respect to corrosion in all but highly alkaline environments.[9]

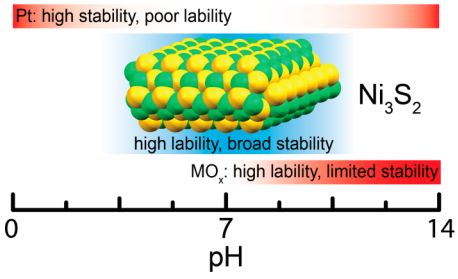

Figure 1. pH regimes of activity and stability for Pt, first-row transition metal oxide (MO_x), and Ni_3S_2 ORR catalysts.

Unlike metal oxides, bonding in transition metal sulfides is more covalent, inhibiting their corrosion under similar conditions.[10] Thus, we envisioned that both of the above requirements could be met if a labile first-row transition metal active site ion can be exposed at the surface of a sulfide host lattice. Here, we illustrate the effectiveness of this design strategy by uncovering a novel earth-abundant catalyst for oxygen reduction at neutral pH, the heazlewoodite phase of nickel sulfide, Ni_3S_2. Under phosphate-buffered neutral pH conditions, Ni_3S_2 outperforms state of the art ORR catalysts including MnO_x and platinum owing to its unique combination of labile active sites and corrosion-resistant sulfide lattice.

To probe accurately the specific catalytic activity of Ni_3S_2, we prepared conformal thin films on gold electrodes via layer-by-layer electrodeposition. The resulting films reflect the surface area of the underlying substrate, allowing for straightforward comparisons between materials of different composition and phase. Adapting literature methods,[11] a planar polycrystalline gold electrode was exposed to 2.2 mM NaSH in 0.25 M $(NH_4)_2SO_4$, generating a spontaneous adlayer of sulfur.[12] To desorb excess sulfur from the adlayer, the electrode was subjected to controlled-potential electrolysis at 0.03 V. (All potentials are reported versus the reversible hydrogen electrode, RHE.) Subsequent polarization of this sulfur-modified gold substrate in 10 mM borate electrolyte containing 5 mM Ni^{2+} resulted in the self-limiting deposition of a Ni adlayer. Repeated deposition cycles of sulfur and Ni following this same procedure gave rise to thin films of nickel sulfide coating the gold electrode substrate.

To evaluate the nickel sulfide film morphology, we analyzed films prepared from 25 deposition cycles of Ni and S by cross-sectional SEM (Figure 2A). Field-emission SEM (FE-SEM) images reveal the underlying Si wafer, Ti adhesion layer, and evaporated Au film in high contrast. On top of the Au layer, a 40 nm region of low contrast corresponding to the nickel sulfide thin film is observed. Importantly, the low-contrast region

Received: April 4, 2015
Published: June 23, 2015

DOI: 10.1021/jacs.5b03426
J. Am. Chem. Soc. 2015, 137, 7978−7981

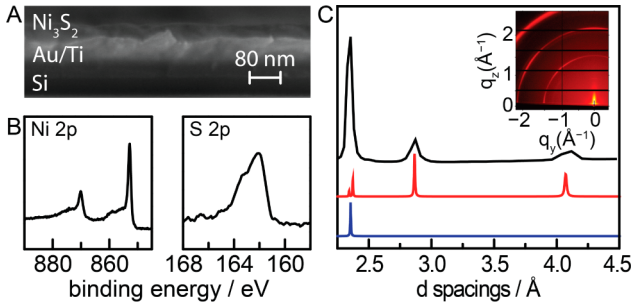

Figure 2. (A) FE-SEM of a Ni_3S_2 thin film prepared from 25 deposition cycles. (B) High-resolution XPS spectra of the Ni 2p and S 2p regions of a Ni_3S_2 film prepared from 10 deposition cycles following argon sputtering to remove adventitious surface oxides. (C) Integration of grazing incidence X-ray diffraction data (inset) obtained on a Ni_3S_2 thin film prepared from 50 deposition cycles (black line). Simulated powder patterns for Ni_3S_2 (red line)[13] and Au (blue line)[14] are shown for comparison.

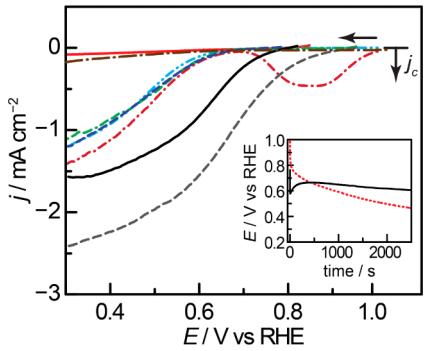

Figure 3. Linear-sweep voltammograms of a Ni_3S_2 thin film prepared from 10 deposition cycles (solid black line), platinum (dashed black line), gold (green line), MnO_x (dashed and dotted red line), NiO_x (cyan line), CoO_x (brown line), and Co_9S_8 (blue line) recorded at 5 mV s^{-1} in O_2-saturated 1 M sodium phosphate electrolyte, pH 7. Linear-sweep voltammogram of a Ni_3S_2 thin film (solid red line) in N_2-saturated 1 M sodium phosphate electrolyte, pH 7. Inset: galvanostatic polarization traces at 0.25 mA cm^{-2} for a platinum (dotted red line) and Ni_3S_2 (solid black line) electrode. All data recorded at 2000 rpm on a rotating disk electrode.

exhibits uniform thickness across the sample with surface undulations that mirror those of the Au underlayer, indicating conformal growth of the nickel sulfide thin film.

The electrodeposited films were analyzed by XPS and grazing incidence diffraction to probe their surface composition and phase. XPS analysis of the as-deposited thin films (Figure S1) reveals three peaks in the Ni $2p^{3/2}$ region at 861.4, 856.0, and 852.8 eV and three peaks in the Ni $2p^{1/2}$ region at 879.3, 873.4, and 870.6 eV (Figure S2). Likewise, two peaks are observed in the S 2p region of the XPS at 161.5 and 162.5 eV (Figure S2). Upon argon sputtering to remove the top surface layers of the film, the Ni 2p region collapses to a single set of peaks at 852.8 eV (Ni $2p^{3/2}$) and 870.0 eV (Ni $2p^{1/2}$), and the S 2p region collapses to a single peak at 162 eV (Figure 2B). Additionally, upon argon sputtering, the O 1s peak intensity dramatically diminishes (Figure S3). Together, these observations are consistent with a thin surface oxide layer coating a uniform nickel sulfide thin film. Integration of Ni and S XPS peaks reveals a Ni/S ratio of ~3:2, implying a Ni_3S_2 empirical formula for the electrodeposited thin film.

To gain further insight into the structure of the electrodeposited thin film, we analyzed electrodes modified with 50 deposition cycles of Ni and S by synchrotron grazing incidence X-ray diffraction (Figure 2C). Three diffuse rings are observed across the detector area (Figure 2C, inset) consistent with a polycrystalline thin film that lacks significant preferred orientation on the gold substrate. Integration of the diffuse rings gives rise to a diffraction pattern with prominent peaks at 2.4, 2.9, and 4.1 Å *d* spacing (Figure 2C). These peaks correspond to the 003, 110, and 111 lattice planes, respectively, of the heazlewoodite phase of nickel sulfide (Ni_3S_2)[13] with overlapping diffraction from the Au 111 lattice plane of the underlying substrate at 2.4 Å *d* spacing. These data, taken together with the 3:2 ratio of Ni/S observed by XPS, indicate that this deposition method generates conformal Ni_3S_2 thin films.

As prepared, the electrodeposited Ni_3S_2 thin films are highly active electrocatalysts for oxygen reduction to water at neutral pH. Slow scan (5 mV/s) linear sweep voltammograms of a Ni_3S_2 thin film prepared from 10 deposition cycles of Ni and S recorded in oxygen-saturated 1 M sodium phosphate, pH 7 (NaP_i electrolyte; Figure 3, solid black line) reveal onset of catalysis at ~0.80 V and display 1 mA cm^{-2} (all currents normalized to the geometric surface area of the electrode) at ~0.61 V, beyond which the catalytic current begins to plateau because of transport limitations. In the absence of O_2, only background double-layer charging current is observed (Figure 3, red solid line), indicating that the catalytic current is solely due to oxygen reduction mediated by the Ni_3S_2 thin film.

Under these electrolyte conditions, the activity of Ni_3S_2 exceeds that of other common precious and base metal oxygen reduction catalysts. Ni_3S_2 films display catalytic onset ~0.1 V more positive than both polycrystalline gold (Figure 3, green line) and Co_9S_8 thin films (blue line),[15] the latter viewed to be among the most active transition metal chalcogenide catalysts for oxygen reduction.[16] In neutral pH phosphate-buffered electrolyte, Ni_3S_2 films also display superior activity relative to first-row transition metal oxides commonly employed in alkaline media. Utilizing known anodic deposition protocols, thick, amorphous NiO_x,[17] MnO_x,[18] and CoO_x[19] films were prepared on gold substrates. Following annealing at 500 °C for 3 h in air, the films were tested for ORR activity in O_2-saturated NaP_i electrolyte. LSV scans of NiO_x (Figure 3, cyan line) and MnO_x (Figure 3, dashed and dotted red line) films reveal catalytic waves with onsets at ~0.7 V, largely indistinguishable from the native activity of the Au substrate. Mn oxide films also exhibit a reductive wave at 0.85 V prior to onset of ORR catalysis (Figure 3, dashed and dotted red line). This prewave is only observed on the first LSV scan of a freshly prepared MnO_x film, and subsequent scans display features that are indistinguishable from those of the Au background (Figure S4). On the basis of the Pourbaix diagram of Mn in water,[9] we attribute the prewave to the reduction of Mn_2O_3 to $Mn^{2+}_{(aq)}$. These results, coupled with the visible loss of both Mn and Ni oxide films from the electrode surface following CV cycling, indicate that these oxides rapidly corrode under reductive polarization in neutral phosphate electrolyte. In contrast, LSV scans of CoO_x films (Figure 3, brown line) reveal negligible initial ORR activity that improves slightly upon CV cycling (Figure S5), suggesting that this oxide is slightly more corrosion-resistant but is nonetheless catalytically inert under these conditions.

Ni_3S_2 films also outperform polycrystalline platinum under identical conditions. Initial slow-scan linear-sweep voltammograms of a polycrystalline platinum-disk electrode reveal catalytic

DOI: 10.1021/jacs.5b03426
J. Am. Chem. Soc. 2015, 137, 7978−7981

onset at ~0.90 V, requiring ~0.1 V lower overpotential than Ni_3S_2 to catalyze ORR at comparable current densities. However, long-term electrolyses reveal that this enhanced activity is transient. Constant current polarization of a Ni_3S_2 film at 0.25 mA cm^{-2} reveals a slight initial rise in activity following double-layer charging, after which the film carries out ORR catalysis at steady state, reaching a potential of 0.59 V at the end of 1 h (Figure 3 inset, solid black line). In contrast, the potential required to maintain the same current density on Pt rapidly and progressively declines over the same time frame (Figure 3 inset, dotted red line). Within 10 min of polarization, the activity of polycrystalline platinum decays beyond that of Ni_3S_2 and requires 140 mV more overpotential to sustain the same catalytic rate after 1 h of constant electrolysis. This activity fade is also observed for high-surface-area Pt/C catalysts (Figure S6). In line with literature reports of strong phosphate adsorption to platinum surfaces,[7] we attribute the decay of its ORR activity to progressive poisoning of the Pt surface by phosphate, a deactivation pathway that Ni_3S_2 resists, allowing it to maintain high activity.

Our observation of high ORR activity from Ni_3S_2 contrasts previous literature reports suggesting that cobalt sulfides are superior catalysts relative to their nickel analogs.[10,20] To gain insight into the mechanistic basis for the opposite trend observed here, we constructed Tafel plots of overpotential versus the log of the activation-controlled current density for ORR (Figure 4) for

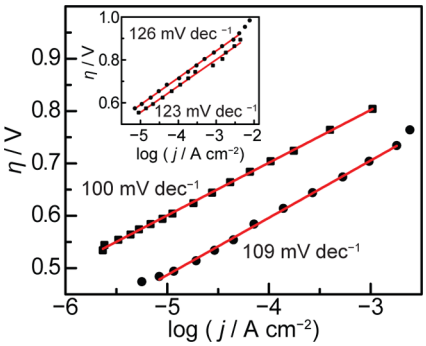

Figure 4. Applied overpotential versus steady-state current density (Tafel plots) for ORR on Ni_3S_2 (●) and Co_9S_8 (■) thin-film electrodes prepared from 10 deposition cycles. Data recorded in O_2-saturated 1 M sodium phosphate, pH 7, at 2000 rpm. Inset: Tafel plots of Ni_3S_2 (●) and Co_9S_8 (■) thin films recorded in O_2-saturated 0.1 M $HClO_4$ at 2000 rpm.

thin films of Ni_3S_2 and Co_9S_8, the latter viewed to be the most active phase of cobalt sulfide.[16] To account for transport limitations at higher overpotentials, we extrapolated Koutecky–Levich plots of reciprocal current density, j^{-1}, versus the reciprocal square root of the rotation rate, $\omega^{-1/2}$, to the y axis, representing infinite rotation rate (representative Koutecky–Levich plots, Figure S7).[21] The resulting Tafel plots (Figure 4) exhibit linear regions spanning 2.5 decades of current density and nearly 0.3 V in potential. Over this linear region, slopes of 109 and 100 mV $decade^{-1}$ are observed for Ni_3S_2 and Co_9S_8, respectively, indicating that both proceed via rate-limiting one-electron transfer to O_2.[21]

Despite a common mechanistic profile, Ni_3S_2 outperforms Co_9S_8 by ~1 order of magnitude over the entire range of Tafel data collection at pH 7. In contrast, Ni_3S_2 and Co_9S_8 display similar activity in 0.1 M $HClO_4$ (Figure 4, inset) and slightly higher Tafel slopes of 126 and 123 mV $decade^{-1}$, respectively, indicative of a common rate-limiting one-electron transfer step of catalysis with a slightly lower transfer coefficient, 0.5 at pH 1 versus 0.6 at pH 7. Thus, although Co_9S_8 exhibits a nearly Nernstian pH dependence, giving rise to similar overpotentials independent of the electrolyte pH (Figure S8), Ni_3S_2 exhibits a sub-Nernstian pH dependence, giving rise to higher activity as the pH increases (Figure S9). The precise origin of these divergent pH dependencies is the subject of ongoing investigations. Notwithstanding, these data indicate that Ni_3S_2's superior activity at intermediate pH arises from a nonclassical pH dependence on the reaction rate.

To probe the selectivity of Ni_3S_2 for direct four-electron reduction of O_2 to water, we utilized rotating ring-disk electrode (RRDE) voltammetry. In this technique, oxygen is reduced at a rotating disk electrode modified with a Ni_3S_2 thin film, and any peroxide generated is oxidized back to O_2 at a concentric Pt-ring electrode, allowing for direct quantification of the current efficiency for four-electron reduction of O_2 to water. As seen in Figure 5, low currents are observed on the ring electrode over a

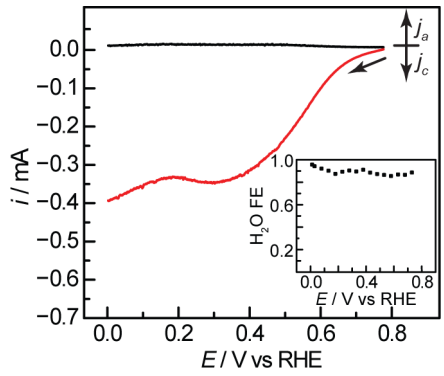

Figure 5. Rotating ring-disk linear-sweep voltammetry recorded at 5 mV s^{-1} in O_2-saturated 1 M sodium phosphate electrolyte, pH 7. Disk current (solid red line) for O_2 reduction on a Ni_3S_2 thin film prepared from 10 deposition cycles and ring current (solid black line) for peroxide oxidation. Inset: faradaic efficiency for H_2O production from O_2 reduction.

wide potential range spanning the catalytic wave, corresponding to ~90% faradaic efficiency for O_2 reduction to water (Figure 5, inset).[22] This value is corroborated by the similarity in slopes of Koutecky–Levich plots of diffusion-limited currents for Ni_3S_2 and Pt, a known four-electron O_2 reduction catalyst (Figure S10).[23]

The promising catalytic activity observed for Ni_3S_2 thin films described above can be translated to nanoparticle systems. Nanocrystalline Ni_3S_2 was prepared on Vulcan carbon XC-72R by refluxing a 1,5-pentanediol solution of $Ni(acac)_2$ and cystamine dihydrochloride in the presence of the Vulcan carbon support. The procedure generates 10–50 nm Ni_3S_2 nanoparticles dispersed on the carbon support with a minor NiS impurity phase that is known to be a poor catalyst for the ORR under these conditions.[20a] This carbon/Ni_3S_2 composite, designated Ni_3S_2@C, was dispersed in ethanol, combined with a nafion binder, and drop-cast onto a glassy-carbon rotating disk electrode at a Ni_3S_2 loading of 0.23 mg cm^{-2}. (See Supporting Information for details of catalyst loading determination.) The composite film was tested for catalytic activity in O_2-saturated NaP_i electrolyte (Figure 6). Consistent with the higher surface area of Ni_3S_2 in this carbon composite, current densities of 0.5 mA cm^{-2} are observed at ~0.75 V, 85 mV lower overpotential

DOI: 10.1021/jacs.5b03426
J. Am. Chem. Soc. 2015, 137, 7978–7981

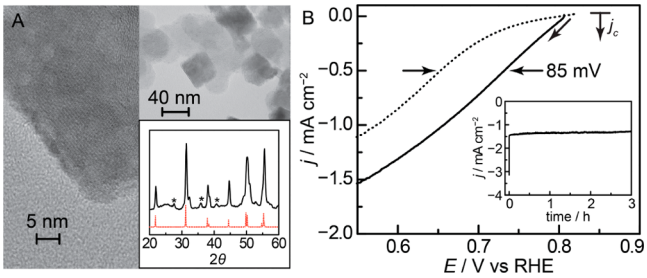

Figure 6. (A) HR-TEM of Ni_3S_2@C. Inset: X-ray diffraction pattern of the prepared Ni_3S_2 (solid black line) and a pattern simulated from literature data (dotted red line).[13] Stars denote a minor NiS impurity phase. (B) Linear sweep voltammograms of a drop-cast film of Ni_3S_2@C on a glassy-carbon rotating disk electrode (solid line) and a Ni_3S_2 thin film (dotted line) in O_2-saturated 1 M sodium phosphate electrolyte, pH 7, rotated at 2000 rpm. Inset: constant potential electrolysis of Ni_3S_2@C at 0.48 V.

than that required for Ni_3S_2 thin films. Importantly, Ni-doped carbon composites prepared using identical synthetic conditions but with exclusion of the sulfur precursor display negligible activity (Figure S11), indicating that catalysis arises from Ni_3S_2 rather than Ni sites adsorbed on the carbon itself. The activity of the Ni_3S_2@C composite remains unchanged over a 3 h course of controlled potential electrolysis at 0.48 V (Figure 6, inset), highlighting the stability of this material in phosphate-buffered neutral pH electrolyte.

We have identified a new, highly active, earth-abundant oxygen reduction catalyst, Ni_3S_2, that operates effectively at neutral pH. Unlike first-row transition metal oxides and Pt, Ni_3S_2 resists corrosion and poisoning in phosphate-buffered neutral pH electrolytes, and its superior performance relative to Co_9S_8 arises from a non-Nernstian pH dependence of oxygen reduction activity. These results, coupled with the observation of robust catalysis from carbon-supported Ni_3S_2 nanoparticles, suggest that Ni_3S_2 is an ideal candidate for oxygen reduction under intermediate pH conditions, potentially enabling the use of lower-cost cell components and biological oxidation catalysts in functional devices.[24]

■ ASSOCIATED CONTENT

Supporting Information

Full experimental details, additional voltammograms, Koutecky–Levich plots, and XPS spectra. The Supporting Information is available free of charge on the ACS Publications website at DOI: 10.1021/jacs.5b03426.

■ AUTHOR INFORMATION

Corresponding Author

*yogi@mit.edu

Notes

The authors declare no competing financial interest.

■ ACKNOWLEDGMENTS

We gratefully acknowledge Sophie Liu, Anthony Hall, and Joe Strzalka for assistance with gold electrode fabrication, SEM data collection, and GIXD data collection, respectively. This research was supported through a Research Agreement with Saudi Aramco, a Founding Member of the MIT Energy Initiative, by the NSF under award CHE-1454060, and by the MIT Department of Chemistry through junior faculty funds for Y.S. This work made use of the MRSEC Shared Experimental Facilities at MIT, which is supported in part by the NSF under award DMR-0819762.

■ REFERENCES

(1) (a) Katsounaros, I.; Cherevko, S.; Zeradjanin, A. R.; Mayrhofer, K. J. J. *Angew. Chem., Int. Ed.* **2014**, *53*, 102−121. (b) Lewis, N. S.; Nocera, D. G. *Proc. Natl. Acad. Sci. U.S.A.* **2006**, *103*, 15729−15735. (c) Gewirth, A. A.; Thorum, M. S. *Inorg. Chem.* **2010**, *49*, 3557−3566.

(2) Umena, Y.; Kawakami, K.; Shen, J.-R.; Kamiya, N. *Nature* **2011**, *473*, 55−60.

(3) (a) Ferguson-Miller, S.; Babcock, G. T. *Chem. Rev.* **1996**, *96*, 2889−2907. (b) Collman, J. P.; Devaraj, N. K.; Decréau, R. a; Yang, Y.; Yan, Y.-L.; Ebina, W.; Eberspacher, T. A.; Chidsey, C. E. D. *Science* **2007**, *315*, 1565−1568.

(4) Solomon, E. I.; Chen, P.; Metz, M.; Lee, S.-K.; Palmer, A. E. *Angew. Chem., Int. Ed.* **2001**, *40*, 4570−4590.

(5) Wen, Z.; Ci, S.; Zhang, F.; Feng, X.; Cui, S.; Mao, S.; Luo, S.; He, Z.; Chen, J. *Adv. Mater.* **2012**, *24*, 1399−1404.

(6) (a) Carver, C.; Matson, B.; Mayer, J. *J. Am. Chem. Soc.* **2012**, *134*, 5444−5447. (b) Rosenthal, J.; Nocera, D. G. *Acc. Chem. Res.* **2007**, *40*, 543−553.

(7) (a) Wang, J. X.; Markovic, N. M.; Adzic, R. R. *J. Phys. Chem. B* **2004**, *108*, 4127−4133. (b) Li, Q.; Wu, G.; Cullen, D. A.; More, K. L.; Mack, N. H.; Chung, H.; Zelenay, P. *ACS Catal.* **2014**, *4*, 3193−3200. (c) He, Q.; Shyam, B.; Nishijima, M.; Ramaker, D.; Mukerjee, S. *J. Phys. Chem. C* **2013**, *117*, 4877−4887. (d) He, Q.; Yang, X.; Chen, W.; Mukerjee, S.; Koel, B.; Chen, S. *Phys. Chem. Chem. Phys.* **2010**, *12*, 12544−12555.

(8) (a) Helm, L.; Merbach, A. E. *Chem. Rev.* **2005**, *105*, 1923−1959. (b) Taube, H. *Chem. Rev.* **1952**, *50*, 69−126.

(9) Pourbaix, M. *Atlas of Electrochemical Equilibria in Aqueous Solutions*; National Association of Corrosion Engineers: Houston, TX, 1974.

(10) Bouroushian, M. *Electrochemistry of Metal Chalcogenides*; Springer-Verlag: Berlin, 2010.

(11) Loglio, F.; Innocenti, M.; Jarek, A.; Caporali, S.; Pasquini, I.; Foresti, M. L. *J. Electroanal. Chem.* **2010**, *638*, 15−20.

(12) Gregory, B. W.; Stickney, J. L. *J. Electroanal. Chem.* **1991**, *300*, 543−561.

(13) Parise, J. B. *Acta Crystallogr., Sect. B* **1980**, *36*, 1179−1180.

(14) Couderc, J. J.; Garigue, G.; Lafourcade, L.; Nguyen, Q. T. *Z. Metallkd.* **1959**, *50*, 708−716.

(15) Falkowski, J.; Surendranath, Y. *ACS Catal.* **2015**, *5*, 3411−3416.

(16) Sidik, R. A.; Anderson, A. B. *J. Phys. Chem. B* **2006**, *110*, 936−941.

(17) Bediako, D. K.; Lassalle-Kaiser, B.; Surendranath, Y.; Yano, J.; Yachandra, V. K.; Nocera, D. G. *J. Am. Chem. Soc.* **2012**, *134*, 6801−6809.

(18) Huynh, M.; Bediako, D. K.; Nocera, D. G. *J. Am. Chem. Soc.* **2014**, *136*, 6002−6010.

(19) Surendranath, Y.; Kanan, M. W.; Nocera, D. G. *J. Am. Chem. Soc.* **2010**, *132*, 16501−16509.

(20) (a) Kishi, T.; Shimizu, F.; Nagai, T. *Surf. Technol.* **1984**, *21*, 109−115. (b) Iwaya, W.; Takase, S.; Shimizu, Y. *Electrochem. Commun.* **2011**, 364−366. (c) Zhu, L.; Susac, D.; Teo, M.; Wong, K.; Wong, P.; Parsons, R.; Bizzotto, D.; Mitchell, K.; Campbell, S. *J. Catal.* **2008**, *258*, 235−242.

(21) Gileadi, E. *Physical Electrochemistry, Fundamentals, Techniques and Applications*; Wiley-VCH: Weinheim, Germany, 2011.

(22) Albery, W. J.; Hitchman, M. L. *Ring-Disk Electrodes*; Oxford University Press: London, 1971.

(23) Strbac, S. *Electrochim. Acta* **2011**, *56*, 1597−1604.

(24) (a) Rismani-Yazdi, H.; Carver, S. M.; Christy, A. D.; Tuovinen, O. H. *J. Power Sources* **2008**, *180*, 683−694. (b) Yang, J.; Ghobadian, S.; Goodrich, P. J.; Montazami, R.; Hashemi, N. *Phys. Chem. Chem. Phys.* **2013**, *15*, 14147−14161. (c) Leech, D.; Kavanagh, P.; Schuhmann, W. *Electrochim. Acta* **2012**, *84*, 223−234.

DOI: 10.1021/jacs.5b03426
J. Am. Chem. Soc. 2015, 137, 7978−7981